LC-PHSM-2008-006

A Clustering Algorithm for the Luminosity Calorimeter

H. Abramowicz, R. Ingbir, S. Kananov, A. Levy, I. Sadeh

School of Physics and Astronomy, The Raymond and Beverly Sackler Faculty of Exact Sciences, Tel Aviv University, Tel Aviv, Israel.

On behalf of the FCAL collaboration

September 2008

The linear collider community has set a goal to achieve a relative precision of 10^{-4} on the luminosity measurement at the ILC. This may be accomplished by constructing a finely granulated calorimeter, which will measure Bhabha scattering at small angles. The Bhabha cross-section is theoretically known to great precision, yet the rate of Bhabha scattering events, which would be measured by the luminosity detector, will be influenced by beam-beam effects, and by the inherent energy spread of the collider. The electroweak radiative effects can be calculated to high precision and partially checked with events with final state photon radiation by distinguishing between the observable energy deposits of electrons and of photons in the luminosity calorimeter. Here the first attempt to perform clustering in the luminosity calorimeter is presented.

1 Introduction

The focus of this study is the luminosity calorimeter (LumiCal) of the International Linear Collider (ILC). The requirement for LumiCal is to enable a measurement of the integrated luminosity with a relative precision of about 10^{-4} [1]. Bhabha scattering is used as the gauge process for the luminosity measurement. This is motivated by the fact that the cross-section of Bhabha scattering is large and dominated by electromagnetic processes, and thus can be calculated with very high precision [2, 3, 4, 5, 6].

Figure 1 shows the Feynman diagrams of the s- and t-channel Born-level elastic Bhabha scattering process, $e^+e^- \to e^+e^-$.

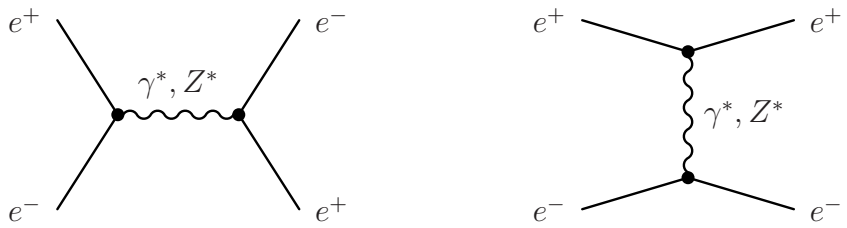

(a) s channel (b) t channel

Figure 1: Feynman diagrams of the (a) s- and (b) t-channel Born-level elastic Bhabha scattering.

Strictly speaking, Born-level elastic Bhabha scattering never occurs. In practice, the process is always accompanied by the emission of electromagnetic radiation, for example,

$$e^+e^- \to e^+e^-\gamma. \tag{1}$$

In a simplified picture, a Bhabha event may be depicted as occurring in three steps: emission of radiation from the initial particles, Bhabha scattering and emission of radiation from the final particles. The ability to distinguish between a radiative photon, which enters LumiCal, and its accompanying lepton is determined by the resolving capabilities of the detector, and is a function of the angular separation between the two particles and of the energy of each particle.

For small angles ($\leq 10°$), Bhabha scattering is dominated by the t-channel exchange of a photon [7]. One can write the differential of the cross-section, σ_{B}, as

$$\frac{d\sigma_{\mathrm{B}}}{d\theta} = \frac{2\pi\alpha_{em}^2}{s}\frac{\sin\theta}{\sin^4(\theta/2)} \approx \frac{32\pi\alpha_{em}^2}{s}\frac{1}{\theta^3}\,, \tag{2}$$

where the scattering angle, θ, is the angle of the scattered lepton with respect to the beam, α_{em} is the fine structure constant, and s is the center-of-mass energy squared.

The typical signature of Bhabha scattering events is the presence of an electron and positron, back to back in the detector. A set of topological cuts is applied by comparing the scattering angles of the electron and of the positron, and by constraining the difference between, and the magnitude of, the energy which is collected in each detector arm [8, 9, 10]. The different systematic contributions to the relative error on the measurement of the integrated luminosity, $\mathcal{L}$, come down to

$$\frac{\Delta\mathcal{L}}{\mathcal{L}} = \frac{\Delta N}{N} = \frac{N_{rec} - N_{gen}}{N_{gen}}\Bigg|_{\theta_{min}}^{\theta_{max}}, \tag{3}$$

where N_{rec} and N_{gen} are respectively the number of reconstructed and generated Bhabha events, and θ_{min} and θ_{max} are the respective low and high bounds on the fiducial volume (acceptance region) of the detector.

At the ILC the colliding electron and positron bunches disrupt one another [11]. Prior to the Bhabha scattering, the interacting particles are likely to have been deflected by the space charge of the opposite bunch, and their energies reduced due to the emission of beamstrahlung. To take into account the cross-section dependence on s, the probability used to produce Bhabha scattering events during the beam-beam collision should be rescaled by s/s', where s' is the effective center-of-mass energy after the emission of beamstrahlung. The variance in s will, in addition, be aggravated by the inherent energy spread of the collider. In general, the collision parameters that lead to the highest luminosity, such as the size of the collision region and the bunch current, also lead to the largest smearing of the luminosity spectrum, $d\mathcal{L}/d\sqrt{s}$. Additionally, the energy measurements can be tempered by the presence of beam related backgrounds, such as synchrotron radiation and thermal photons of the residual gas, backscattered off the electron beam.

The acollinearity angle for the e^+e^- final state, $\theta_{\mathcal{A}}$, is defined as

$$\theta_{\mathcal{A}} \equiv \theta_{e^-} + \theta_{e^+} - \pi. \tag{4}$$

Beamstrahlung emissions often occur asymmetrically, with either the electron or the positron loosing most of the energy. Hence the acollinearity of the final state can be significantly enhanced. The final state particles scattered in the acceptance range of LumiCal, following a Bhabha interaction, can typically cross a significant part of the opposite bunch. They can thus be focused by the electromagnetic field from the corresponding space charge, which causes the scattering angle to change.

Both beamstrahlung emissions and electromagnetic deflections vary with the bunch length, the horizontal bunch size, and the energy of the collision, and hence so do the resulting biases on the integrated luminosity. Reconstructing $d\mathcal{L}/d\sqrt{s}$ from the scattered Bhabha angles is possible [12, 13]. This is done by measuring the acollinearity angle, which is related to the difference in the energies of the electron and positron beams, in

the case of small energy and small scattering angle differences. The luminosity spectrum needs to be unfolded from the rates for the observed signal-channels in order to produce cross-sections as a function of energy. This is especially important for such analyses as top-quark and W-boson mass measurements [14]. Knowing $d\mathcal{L}/d\sqrt{s}$ also provides a good way to measure the amount of beamstrahlung, and thus to predict the corresponding contribution to the bias.

Contrary to the case with beamstrahlung, there is no direct way to control experimentally the bias from the electromagnetic deflections, and so these have to be simulated in order to compensate for their effect.

Since both the beam-beam effects and the collider energy spread depend on the parameters of the collisions, it would be very productive to measure the Bhabha cross-section itself, and thus better control the systematic errors. A direct measurement of the cross-section is not possible. However, the electroweak radiative effects, which can be calculated to high precision, can be partially checked with events with final state photon radiation. This may be done by distinguishing between the observable energy deposits of electrons and of photons in the luminosity calorimeter, using a clustering algorithm.

Here the first attempt to perform clustering in the luminosity calorimeter by means of a dedicated algorithm is presented. This note includes a short introduction, a description of the algorithm and an example of a clustering analysis of a sample of Bhabha events.

2 Simulation of the Detector Response

2.1 The Geometry of LumiCal

LumiCal is a tungsten-silicon sandwich calorimeter. In the present detector concept [15], LumiCal is placed 2.27 m from the interaction point. The LumiCal inner radius is 80 mm, and its outer radius is 350 mm, resulting in a polar angular coverage of 35 to 153 mrad. The longitudinal part of the detector consists of layers, each composed of 3.5 mm of tungsten, which is equivalent to 1 radiation length (defined below) thickness. Behind each tungsten layer there is a 0.6 mm ceramic support, a 0.3 mm silicon sensor plane, and a 0.1 mm gap for electronics. LumiCal comprises of 30 longitudinal layers. The transverse plane is subdivided in the radial and azimuthal directions. The number of radial divisions is 104, and the number of azimuthal divisions is 96. Figure 2 presents the segmentation scheme of a LumiCal sensor plane.

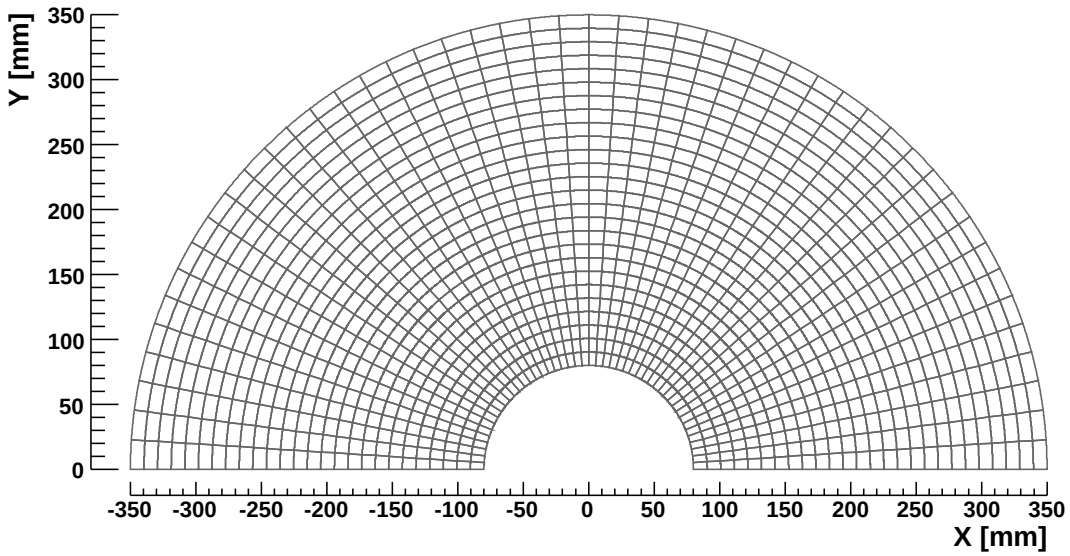

Figure 2: Half plane of LumiCal silicon sensors (every fourth radial segment is drawn).

2.2 Simulation Tools

The response of LumiCal to the passage of particles was simulated using MOKKA, version 06-05-p02 [16]. MOKKA is an application of a general purpose detector simulation package, GEANT4, of which version 9.0.p01 was used [17]. The GEANT4 range-cut parameter was set to 0.005 mm. The MOKKA model chosen was LDC00_03Rp, where LumiCal is constructed by the LumiCalX super driver. The output of MOKKA is in the LCIO format, which may be processed by MARLIN, a C++ software framework for the ILC software [18]. Version 00-09-08 of MARLIN was used.

2.3 Development of Electromagnetic Showers in LumiCal

When a high-energy electron or photon is incident on a thick absorber, it initiates an electromagnetic (EM) shower as pair production and bremsstrahlung generate more electrons and photons with lower energy. The longitudinal development is governed by the high-energy part of the cascade, and scales with the *radiation length* in the material, X_0. The radiation length is defined as the mean distance over which a high-energy electron loses all but 1/e of its energy by bremsstrahlung. Electron energies eventually fall below the critical energy (defined below), and then dissipate their energy by ionization and excitation, rather than by the generation of more shower particles.

Two normalized distributions are overlaid in Fig. 3a, the number of shower particles and the deposited energy in a single layer, both as a function of the layer number, ℓ.

Electron showers of 250 GeV were used. The energy deposited in the silicon sensors is proportional to the number of charged shower particles. This is consistent with the fact that both distributions have a similar shape. However, while the distribution of the number of shower particles peaks at the ninth layer, that of the energy deposition peaks at the tenth. The displacement between the distributions by one layer is due to the fact that part of the shower is comprised of photons which do not deposit energy, but are later converted to electron-positron pairs, which do. In Fig. 3b is presented the normalized distribution of the number of cell hits (cells in which energy was deposited) for 250 GeV electron showers as a function of the layer in LumiCal. The number of cells which register a hit peaks around $\ell = 13$.

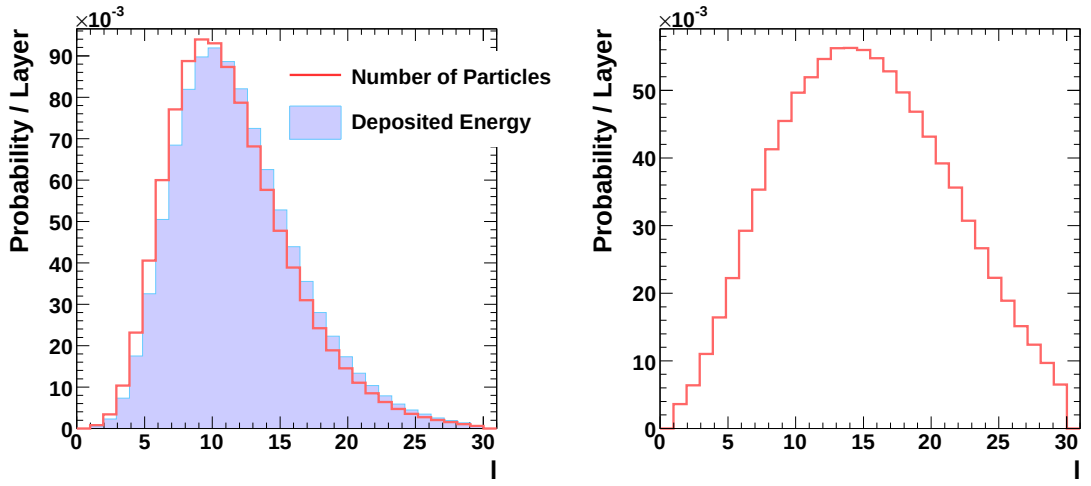

(a) (b)

Figure 3: (a) Normalized distributions of the number of shower particles and of the deposited energy in a single layer, as a function of the layer number, ℓ, as denoted in the figure. Electron showers of 250 GeV were simulated. (b) Normalized distribution of the number of cell-hits for 250 GeV electrons showers as a function of the layer in LumiCal.

The polar and azimuthal angles of a shower, θ and ϕ, are reconstructed by averaging over the individual cells in the detector. For a cell i with center coordinates $\{\theta_i, \phi_i\}$, a weight function, $\mathcal{W}_i$, is used, so that

$$< \alpha >= \frac{\sum_i \alpha_i \cdot \mathcal{W}_i}{\sum_i \mathcal{W}_i}, \tag{5}$$

for $\alpha = \theta, \phi$. Weights are determined by the so-called logarithmic weighting [19], for which

$$\mathcal{W}_i = \max\{\ 0\ ,\ \mathcal{C} + \ln\frac{E_i}{E_{tot}}\}, \tag{6}$$

where E_i is the individual cell energy, E_{tot} is the total energy in all cells, and $\mathcal{C}$ is a constant. In this way, an effective cutoff is introduced on individual hits, and only cells which contain a high percentage of the energy of the shower contribute to the reconstruction. This cut, which depends on the amount of deposited energy, is determined by $\mathcal{C}$.

The polar (azimuthal) resolution, σ_θ (σ_ϕ), and the polar (azimuthal) bias, $\Delta\theta$ ($\Delta\phi$), are, respectively, the root-mean-square and the most probable value of the distribution of the difference between the reconstructed and the generated angles. The existence of the bias is due to the non-linear transformation between the global coordinate system of the detector, and the coordinate system of LumiCal, in which the shower position is reconstructed. There is an optimal value for $\mathcal{C}$ for the reconstruction of θ (ϕ), for which the polar (azimuthal) resolution is minimal [20, 15]. The *global shower-center* is defined as the center of gravity of the shower using the angles θ and ϕ, which are reconstructed with the respective optimal values of $\mathcal{C}$.

The transverse development of electromagnetic showers scales fairly accurately with the Molière radius, $R_{\mathcal{M}}$, given by [21]

$$R_{\mathcal{M}} = X_0\frac{E_s}{E_c}\,, \tag{7}$$

where $E_s \approx 21$ MeV, and E_c is the *critical energy*, which is defined as the energy at which the ionization loss per radiation length is equal to the energy of the shower particles [22]. On average, only 10% of the energy of an EM shower lies outside a cylinder with radius $R_{\mathcal{M}}$ around the global shower-center. Figure 4a shows the distribution of the distance around the global shower-center, in which 90% of the integrated shower energy may be found. The distribution is centered around 14 mm.

Local shower-centers are defined on a layer-to-layer basis as the extrapolation of the trajectory of the particle according to the reconstructed angles. We define the distance around the local shower-center of layer ℓ, in which 90% of the energy of the layer is deposited, as the *layer-radius*, $r(\ell)$, of the layer. Figure 4b shows the dependence of $r(\ell)$ on the layer number. According to the distributions in Fig. 3, in the first layers there are few cells which register hits. For this reason there is no clear local shower-center, and the area that encompasses 90% of the energy of the layer is large. The information in these layers is, therefore, not sufficient to obtain a clear description of the shower. This effect is lessened as the shower develops in depth and the number of cell-hits increases. Starting at the fifth layer, the shower becomes homogeneous. Beyond this point the shower becomes more and more wide-spread in depth, and its diameter may be estimated to good approximation by a power-law. For layer numbers higher than 16, the shower exceeds 150% of $R_{\mathcal{M}}$ and looses homogeneity once again. This behavior

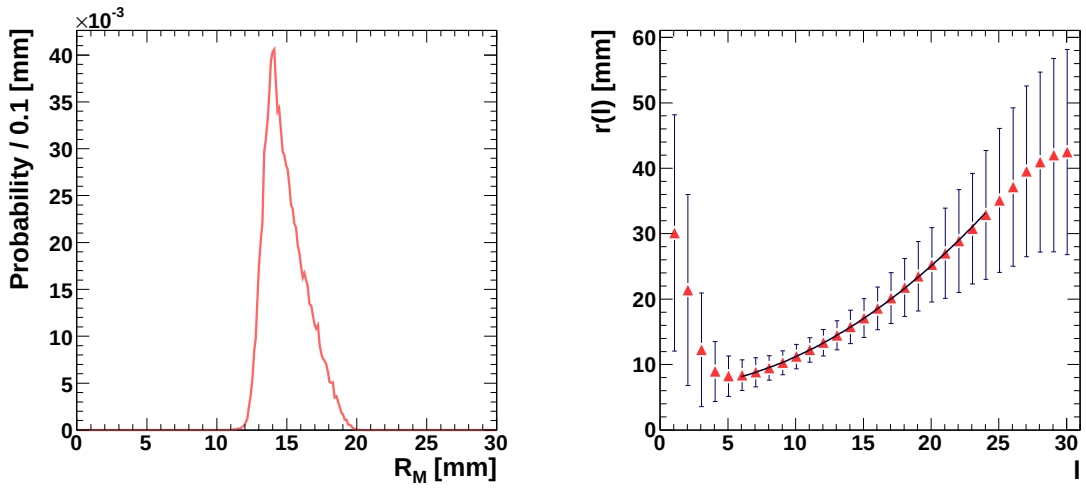

(a) (b)

Figure 4: (a) Distribution of $R_{\mathcal{M}}$, the distance around the global shower-center, in which 90% of the integrated shower energy may be found. (b) Dependence on the layer number, ℓ, of the layer-radius, $r(\ell)$, which is the distance around the local shower-center in which 90% of the energy of the layer is deposited. The curve shows the fit results to a power law of $r(\ell)$ for the region $6 \leq \ell \leq 24$ (Eq. (8)).

is supported by the distributions presented in Fig. 3, which show that for layers beyond the shower-peak, the number of shower-particles falls off faster than the number of cells which are hit. Since the shower becomes attenuated for high values of ℓ, it is difficult to determine the local shower-center with good accuracy. It is useful (see Sect. 3.1.3) to define an *effective layer-radius*, $r_{eff}(\ell)$, by extrapolation of the behavior of $r(\ell)$ at the layers where the shower size is stable, to the rest of the calorimeter,

$$r_{eff}(\ell) \equiv r_\ell(6 \leq \ell \leq 24) \approx 6 + 0.04 \cdot \ell + 0.05 \cdot \ell^2 \ . \tag{8}$$

This relation holds for particles with energy in the range which is important for this study (1 GeV and higher). The reason for this is that the Molière radius is does not depend strongly on the energy of the initiating particle in this energy scale.

Figure 5a shows the profile of the energy deposited in LumiCal for a single 250 GeV electron shower. Integration in each case is made along the z-direction for equivalent values of the θ and ϕ plane coordinates. Figure 5b shows the transverse energy profile for a pair of showers with energies of 230 and 20 GeV. The centers of the two showers are separated by one Molière radius. It is apparent that even if one is able to distinguish between the cores of the showers, many low-energy deposits are going to remain inter-mixed between the pair. It may also be noted that the shape of the energy profile of the convoluted shower-pair appears, as expected, similar to that of the single shower of comparable energy.

In summary, the transverse profile of 250 GeV EM showers in LumiCal is characterized by a peak of the shower around the thirteenth layer. The number of shower-particles before layer six and after layer 16 is small compared to that in the inner layers. The energy deposits decrease in depth and the shower becomes more wide spread. The front layers (layers 1-5) are, therefore, characterized by a small number of concentrated energy deposits. The middle, so-called, *shower-peak layers* (layers 6-16)[I] register large energy contributions, and the back layers (layers 16-30) are characterized by a decreasing number of low-energy shower particles, which deposit little energy in a dispersed manner. The shower has a prominent center. Within $R_{\mathcal{M}}$ (14 mm) of this center most of the energy of the shower is concentrated. On a layer-by-layer basis, most of the energy may be found within an effective layer-radius from the center, which is parametrized by Eq. (8).

3 Description of the Clustering Algorithm

The clustering algorithm which was designed for LumiCal operates in three main phases,

- selection of shower-peak layers, and two-dimensional clustering therein;

[I] On an event-by-event basis the longitudinal profile is not always as smooth as the one represented in Fig. 3a. As a result, the layers in which the shower peaks are not necessarily consecutive.

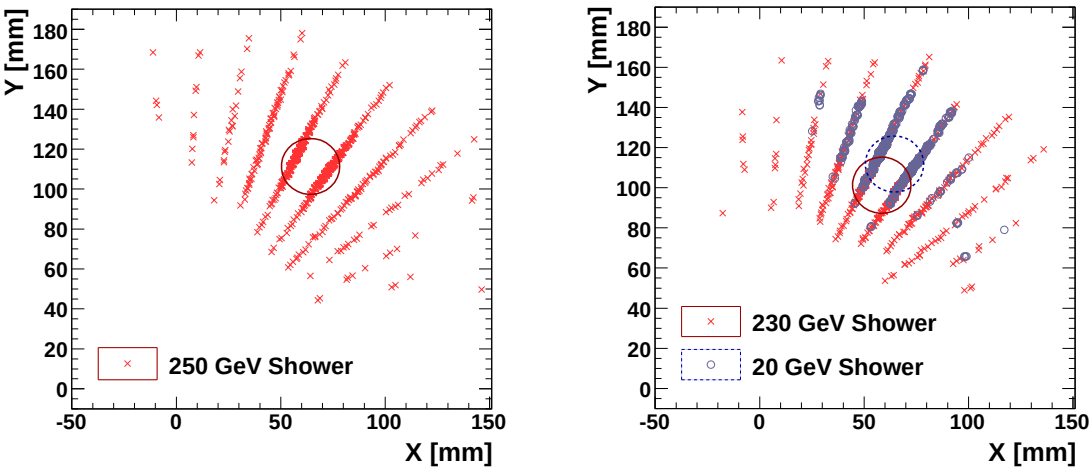

(a) (b)

Figure 5: (a) Transverse energy profile for a 250 GeV electron shower in LumiCal. (b) Transverse energy profile for a pair of electron showers with energies of 230 and 20 GeV, as denoted in the figure. The circles in both figures represent areas bound within one Molière radius around the respective shower-centers.

- fixing of the number of global (three-dimensional) clusters, and collection of all hits onto these;
- characterization of the global-clusters, by means of the evaluation of their energy density.

A short description of each phase will now follow. A complete account can be found in [20]. A C++ code implementation of the algorithm, and a MARLIN interface may be found in [23].

3.1 Clustering in the Shower-Peak Layers

In the first layers of LumiCal, only a few hits from the shower are registered, as was discussed above. In addition to the hits from the main showers, there may also be contributions owing to backscattered particles or background processes. These particles have low energy and do not propagate to the inner layers, but their energy is of the order of the depositions of the showers of interest. In order to make a good estimate of the number of main showers, one must, therefore, begin by considering the information in the shower-peak layers. This process is done in two steps, which are described below, *near-neighbor clustering* and *cluster-merging*.

3.1.1 Near-Neighbor Clustering

Initially, clusters are created from groups of closely-connected cells. This is done by means of the method of near-neighbor clustering (NNC), which exploits the gradient of energy around local shower-centers. The assumption is that in first order, the larger the distance between a hit and the center of the shower, the lower its energy. By comparing the energy distribution around the center at growing distances, one may check whether the energy is increasing or decreasing. An increase in energy for growing distance from the shower-center would then imply that the hit should be associated with a different shower.

For each shower-peak layer separately, the algorithm associates each cell which has an energy deposit with its highest-energy near-neighbor. The result of the NNC phase is a collection of clusters in each layer, centered around local maxima, as illustrated for a single layer in Fig. 6a. In this example the algorithm produces six clusters, which are enumerated in the figure. The different clusters are also distinguished by different color groups, where darker shadings indicate a higher energy content of the cell in question.

3.1.2 Cluster-Merging

The NNC method only connects cells which are relatively close, while showers tend to spread out over a large range of cells, as indicated in Fig. 5. The cluster-merging pro-

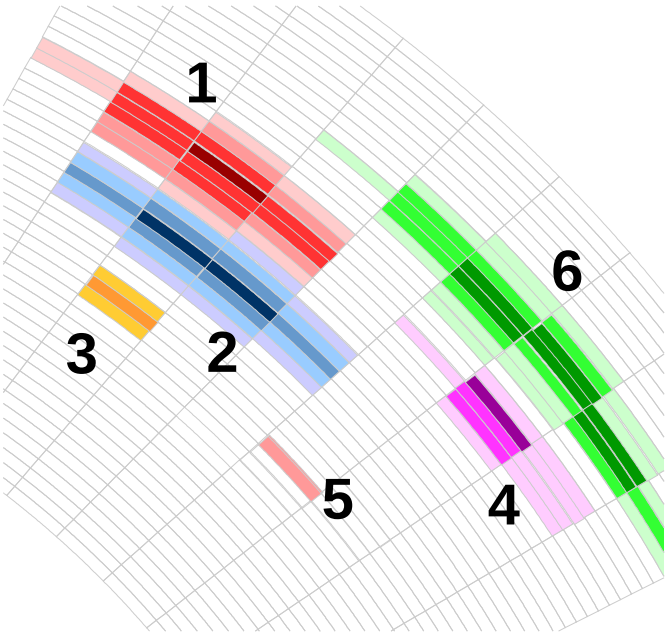

(a)

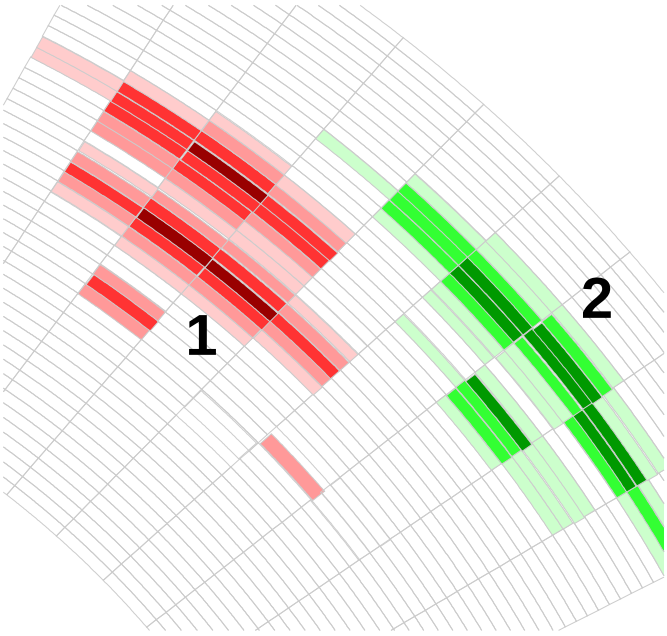

(b)

Figure 6: (a) Schematic representation of the results of the NNC phase for a single layer. Six clusters are found by the algorithm. The different clusters are enumerated, as well as distinguished by different color groups. Darker shadings indicate a higher energy content of the cell in question. (b) Evolution of the results from (a) after the cluster-merging phase. Two clusters remain after clusters two, three and five were merged with cluster one, and cluster four was merged with cluster six.

cedure begins by assigning a center-position to each existing cluster. Weights are then computed for each cluster to merge with the rest of the clusters [20]. In general, the weights are proportional to the energy of the candidate cluster, and inversely proportional to the distance between the pair of clusters. Several variations of the weighting process are tested in consecutive merging attempts. The result of the algorithm after the cluster-merging phase is illustrated for a single layer in Fig. 6b. One can observe that the remaining clusters have well-defined high-energy centers, and that all low-energy residuals have been merged into the large clusters.

3.1.3 Global Clustering

The most important stage of the clustering algorithm is the determination of the number of reconstructed showers. The aftermath of the clustering in the shower-peak layers results in several collections of two-dimensional hit aggregates, the number of which varies from layer to layer. The final number of showers is then determined as the most frequent value of the layer-cluster number, derived from the collections in the shower-peak layers.

Once the number of global-showers is fixed, cells from non-shower-peak layers are associated with one of the global-showers. This is done by extrapolating the propagation of each shower through LumiCal, using the information from the shower-peak layers. Following the extrapolation, cells are merged with the extrapolated global-cluster centers in each layer. This process is facilitated by assuming a typical shower-size, defined according to the parametrization of Eq. (8), which acts as a temporary center-of-gravity. Once the core cells within the assumed shower-radius are associated with the global-centers in these layers, the rest of the cells may also be added. A weighing method, similar to the one used in the shower-peak layers, is used here as well [20].

Figure 7 shows a schematic representation of the global-clustering phase. LumiCal layers are represented by the large blue disks, and layer-clusters are represented by the small triangles, squares and circles. Three layers have two layer-clusters, one layer has three layer-clusters and one layers has one layer-cluster. The first and last layers have no layer-clusters, since they are not shower-peak layers, and so were not taken into consideration in the previous phase of the algorithm. The global number of clusters is two, and the layer clusters are associated with each other according to the straight lines. The lines also define the global-cluster positions in the non-shower-peak layers. The cluster represented by a circle in the layer, in which three layer-clusters were found, will be taken apart. Its hits will be associated with either the “square” or “triangle” global-clusters. The layer-cluster in the layer, in which only one cluster was found, will also be disbanded, since the number of global-clusters is two. The hits will then be clustered around the extrapolated global-cluster center positions, represented by the intersection of the straight lines with the layer. A similar procedure will also be performed in the first and last layers, where no layer-clusters were constructed previously.

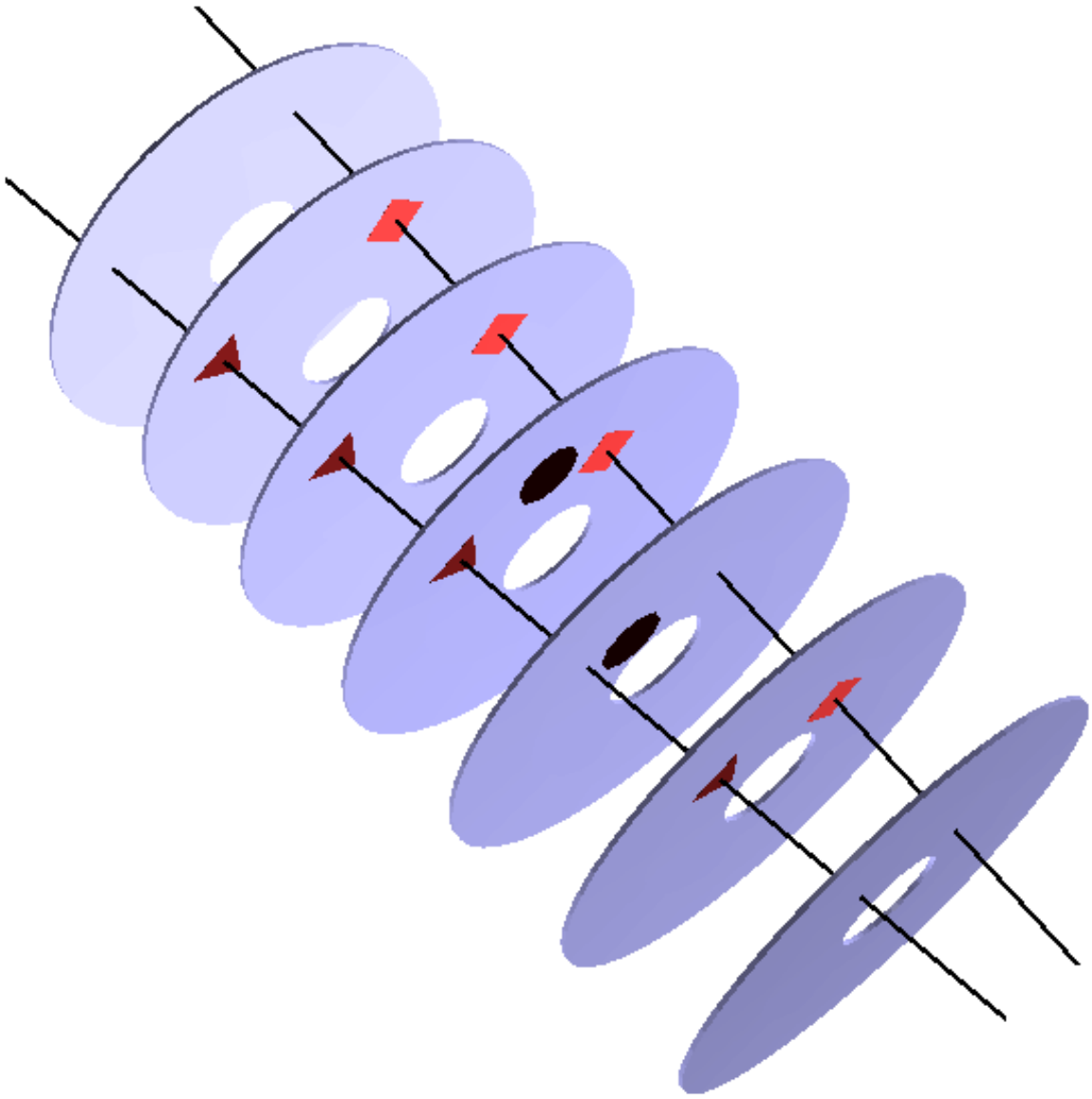

Figure 7: Schematic representation of the global-clustering phase. LumiCal layers are represented by the large blue disks, and layer-clusters are represented by the small triangles, squares and circles. The straight lines show the extrapolated position of the global-clusters in all layers.

3.2 Corrections Based on the Energy Distribution

At this point all of the hits in the calorimeter have been integrated into one of the global-clusters. Before moving on, it is beneficial to make sure that the clusters have the expected characteristics.

3.2.1 Energy Density Test

The development of EM showers in LumiCal has been described in Sect. 2.3. Accordingly, one would expect that 90% of the energy of a cluster would be found within one Molière radius of its center. While statistically this is true, fluctuations may occur on a case-by-case basis, and thus this characteristic of EM showers does not suffice in itself in order to reliably perform the clustering. It is possible to define, instead, a set of tests based on the amount of energy which is located in proximity to each cluster-center [20].

Both the energy-density of individual clusters and the one of all of the clusters together is evaluated. When the global-clusters fall short of the test, a quick re-clustering is attempted. The first step is to integrate the energy in the transverse direction and produce a distribution of cell energy in the longitudinal direction (see Fig. 5). After this is done one may strip away low energy cell contributions and then perform the profiling procedure again in successive iterations. This way, it is sometimes possible to reliably locate the high density shower-centers. Global clusters are then constructed around these centers. The energy density of the new clusters is compared to that of the original clusters, and the best set is finally kept.

3.2.2 Unfolding of Mixed Clusters

Another modification that can be made in the aftermath of the clustering procedure, is allocation of hits for mixed cluster pairs. When a pair of showers develop in close proximity to each other (in terms of their Molière radius), many cells receive energy depositions from both showers. The problem is, that the clustering procedure associates each cell with only one cluster. This biases the energy content, especially for low-energy clusters, due to the fact that their energy tends to be greatly over-estimated by contributions from high-energy clusters (see Fig. 12 below). High-energy clusters are less affected, because percentage-wise, the variance in energy caused by mixed low-energy clusters is insignificant. A way to correct for this effect is to evaluate the energy distribution of each cluster in the region furthest away from the position of its counterpart. If one assumes that the shape of each shower is smooth, the distribution of hits in the area where there is no mixing can be used to predict the distribution in the mixed area[II].

[II] In fact, the assumption of smoothness is not always correct. This is due to statistical fluctuations in the shower development, and also to the fact that the differences of the cell sizes in play are difficult to take into account. Despite this, the method tends to improve the estimation of cluster energy.

Correction factors are then derived on a cell-by-cell basis, and the energy is split between the pair of clusters accordingly.

4 Physics Sample

The physics sample which was investigated consisted of $3 \cdot 10^4$ Bhabha scattering events with center-of-mass energy, $\sqrt{s} = 500$ GeV. The events were generated using BHWIDE, version 1.04 [24]. BHWIDE is a wide angle Bhabha MC, which contains the electroweak contributions, which are important for the high energy e^+e^- interactions considered here. The sample contains only events in which the leptons are scattered within the polar angular range $35 < \theta < 153$ mrad. While all of these events were processed by the clustering algorithm, some were eventually discarded. Only events in which the reconstructed cluster with the highest energy content was found within the fiducial volume of LumiCal, $41.5 < \theta < 131$ mrad[III], were kept. Individual clusters were constrained in the same way.

Figure 8a shows the energy spectrum of the scattered leptons and radiative photons. The lepton distribution peaks at 250 GeV, as expected, and has a long tail of lower energies, accounting for the energy which was carried away by the photons. Figure 8b shows the corresponding distribution of the number of photons in a single event.

Figure 9 shows the polar[IV] and azimuthal production angles, θ and ϕ, of scattered leptons and radiative photons. The distribution of the polar angle is cut according to the fiducial volume of LumiCal. As expected in light of Eq. (2), the distribution of the polar angle falls off rapidly with θ, and the distribution of the azimuthal angle is flat.

The more energy that a photon takes from the lepton, the smaller the angular separation between the two. This is confirmed by Fig. 10a, which shows the correlation between the photon energy and its angular separation from the accompanying lepton, $\Delta\Omega_{\ell,\gamma}$. In Fig. 10b the energy dependence of Fig. 10a is integrated and normalized, showing the likelihood for a radiative photon to have a given distance from its accompanying lepton. The distance in this case is expressed as the separation between the pair of particles on the face of LumiCal in units of mm and of Molière radius. It is apparent from the distributions that the vast majority of radiative photons is of low energy, and enters LumiCal in close proximity to the lepton.

[III] The fiducial volume was determined, such that EM showers of 250 GeV are contained within LumiCal, and the energy resolution is stable [20, 15].

[IV] Naturally the electron and the positron have polar angles of opposite signs, but as the distributions of the production angles are equivalent for either one, this sign will be ignored throughout the following.

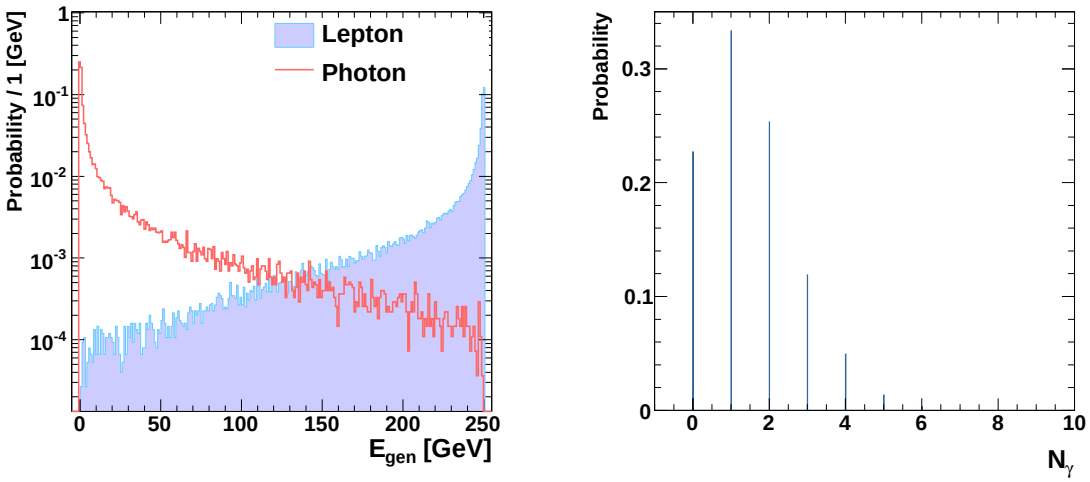

(a) (b)

Figure 8: (a) Distribution of the production energy of scattered leptons and radiative photons, E_{gen}, as denoted in the figure. (b) Distribution of the number of photons in a single event, N_γ. Bhabha scattering events with center-of-mass energy $\sqrt{s} = 500$ GeV were simulated.

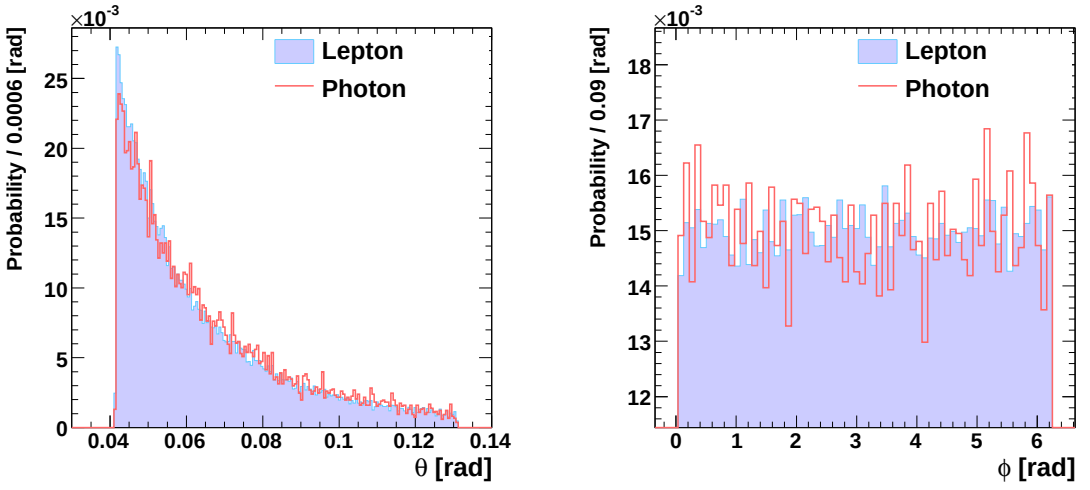

(a) (b)

Figure 9: Distributions of the polar (a) and azimuthal (b) production angles, θ and ϕ, of leptons and photons, as denoted in the figures. The Bhabha scattering events were simulated with center-of-mass energy $\sqrt{s} = 500$ GeV, and the lepton distributions were cut according to the LumiCal fiducial volume.

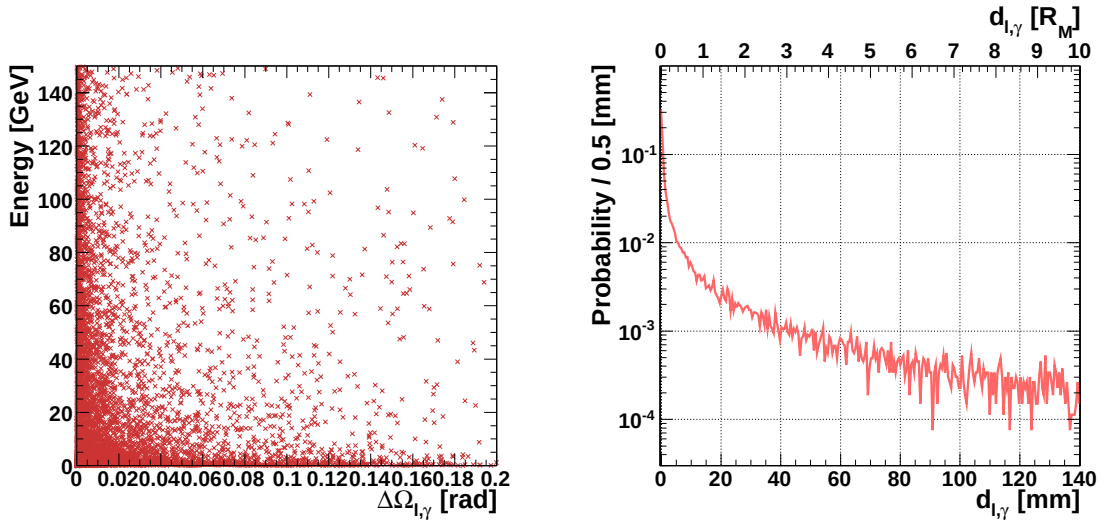

(a) (b)

Figure 10: (a) Correlation between the angular separation between leptons and radiative photons, $\Delta\Omega_{\ell,\gamma}$, and the photon energy. The spectrum of particles is generated for Bhabha scattering with center-of-mass energy $\sqrt{s} = 500$ GeV in the LumiCal fiducial volume. (b) The likelihood for a radiative photon to have a given distance from its accompanying lepton. The distance in this case is expressed in units of mm, as the separation between the pair of particles on the face of LumiCal, $d_{\ell,\gamma}$. An equivalent scale is also shown in units of the Molière radius, $R_{\mathcal{M}}$.

5 Performance of the Clustering Algorithm

The distributions for the position and energy presented in the previous section were drawn from the raw output of the BHWIDE event generator. As such, they represent an ideal description of Bhabha scattering. In reality, observables are distorted by the inherent resolution of the measuring device. The energy resolution, which is determined by the amount of leakage, and by the sampling rate of the calorimeter (see [20, 15]), incurs an error on the signal-to-energy calibration of LumiCal. Similarly, the polar and azimuthal reconstructed angles have a resolution and a bias of their own, as described above. In order to analyze the output of the clustering algorithm it is necessary to isolate the errors in reconstruction resulting from the clustering, from the other systematic uncertainties of LumiCal.

To this effect, two classes of objects may be defined. The basic simulation-truth data will be represented by collections, which contain all of the hits which belong to an EM shower initiated by a single particle. These will be referred to as *generated showers*. Since a single detector cell may contain contributions from more than one EM shower, generated showers may share cells. Hit collections built by the clustering algorithm, will be referred to as *reconstructed clusters*. In order to remove the systematic uncertainties, the properties of both the showers and of the clusters are reconstructed in the same manner, using information from the detector cells.

Since there is no way to distinguish in practice between EM showers initiated by leptons and those started by photons, reconstructed clusters and generated showers will be referred to as having either *high-energy*, or *low-energy*, which correspond to *effective leptons*, and *effective photons*, respectively. High-energy clusters (showers) are identified as those that have the highest integrated energy content among the set of all reconstructed clusters (generated showers). The rest of the clusters (showers) are identified as low-energy clusters (showers).

5.1 Event Selection

Figure 11 shows the success and failure of the clustering algorithm in distinguishing between a pair of generated showers as a function of the separation distance between the pair, d_{pair}, and of the energy of the low-energy shower, E_{low}. Failure of the algorithm may take two forms. A pair of generated showers may be merged into one reconstructed cluster (Fig. 11a), or one shower may be split into two clusters (Fig. 11b). As indicated by Fig. 5b, since the great majority of radiative photons enters LumiCal within a small distance from the leptons, separation between the showers of multiple particles is not trivial. The difficulty is enhanced due to the increasing size of showers as they develop in depth in LumiCal (see Fig. 4b). Distinguishing between pairs of showers becomes easier when either E_{low} or d_{pair} increase in value.

It is, therefore, required to set low bounds on the energy of a cluster, and on the

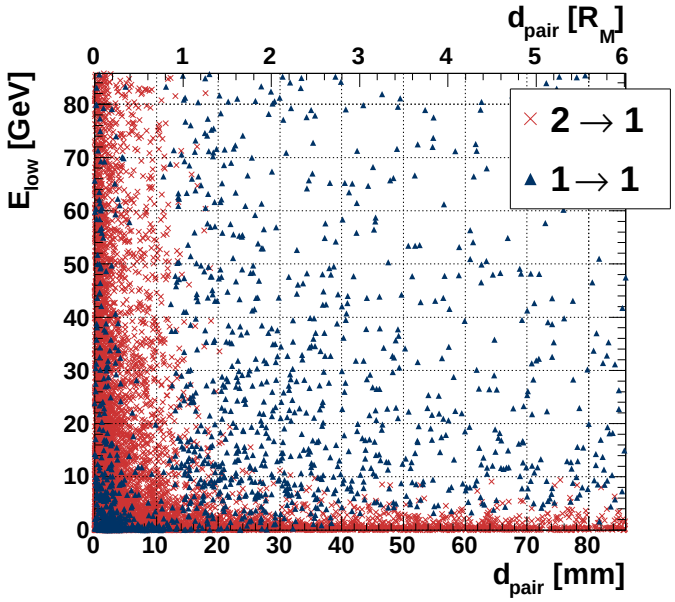

(a)

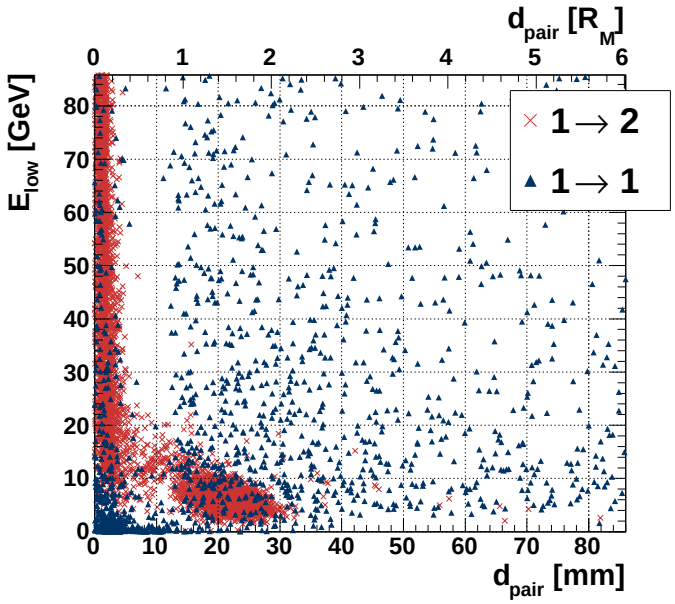

(b)

Figure 11: Success and failure of the clustering algorithm in distinguishing between a pair of generated showers as a function of the separation distance between the pair, d_{pair}, and of the energy of the low-energy shower, E_{low}. The distance d_{pair} is expressed in units of mm and of the Molière radius, $R_{\mathcal{M}}$. Both figures show success ($1 \rightarrow 1$) of the algorithm. (a) also shows cases where a pair of generated showers are merged into one reconstructed cluster ($2 \rightarrow 1$), and (b) also shows cases where a single shower is split into two clusters ($1 \rightarrow 2$).

separation between any pair of clusters. When the algorithm produces results that do not pass the cuts, the two clusters are integrated into one. In order to compare with theory the distribution of clusters after making this *merging-cut* on E_{low} and d_{pair}, one must also apply the same restrictions on the generated showers. After the merging-cut, the generated showers follow a distribution complying with an *effective Bhabha cross-section*.

The distinction between the original and the effective cross-sections is important, and it must be noted that the effective cross-section can only be integrated by simulating the detector response. The position of a cluster is reconstructed by making a cut on cell energy, relative to the entire cluster energy (Eqs. (5) and (6)). As a result, an integration of a pair of clusters into one, sets the position of the merged cluster to an a-priory unpredictable value[V]. The momentum of the initiating particles will, in some cases, not balance with that of the effective (merged) particle. Summing up deposits from multiple showers in LumiCal is, therefore, not equivalent to a naive summation procedure that might be done on the cross-section, at the generated-particle level.

5.2 Observables

5.2.1 Quantification of the Performance

The error on the effective cross-section will depend on the number of miscounted showers. In order to judge the success of the algorithm, one may evaluate its acceptance, $\mathcal{A}$, purity, $\mathcal{P}$, and efficiency, $\mathcal{E}$, which are defined as

$$\mathcal{A} = \frac{N_{1\to1}}{N_{1\to1} + N_{2\to1}}\,, \quad \mathcal{P} = \frac{N_{1\to1}}{N_{1\to1} + N_{1\to2}}\,, \quad \text{and} \quad \mathcal{E} = \frac{\mathcal{A}}{\mathcal{P}}\,, \tag{9}$$

where $N_{1\to1}$ is the number of generated showers which were reconstructed as one cluster by the algorithm, $N_{2\to1}$ is the number of pairs of showers which were reconstructed as one cluster, and $N_{1\to2}$ is the number of single showers which were separated into two reconstructed clusters.

The values of the acceptance, purity and efficiency are presented in Table 1 for several pairs of merging-cuts on the minimal energy and on the separation distance between a pair of clusters. Also shown is the fraction of radiative photons which are available for reconstruction after applying the merging-cuts,

$$\wp_\gamma = \frac{N_\gamma(\text{cut})}{N_\gamma(\text{all})}\,, \tag{10}$$

[V] For instance, if a cluster is of much higher energy than its counterpart, then the energy contributions of the low-energy cluster will not be taken into account in the position reconstruction at all. For the reconstruction of single showers this is not a problem, since the shower is of homogeneous shape around a defined center. For the case of two showers, which are far apart, this is no longer the case.

where N_γ(all) is the total number of radiative photons in the fiducial volume of LumiCal, and N_γ(cut) is the number of photons in LumiCal which also pass the merging-cuts on E_{low} and d_{pair}.

Cuts		$\wp_\gamma$ [%]	$\mathcal{A}$ [%]	$\mathcal{P}$ [%]	$\mathcal{E}$ [%]
d_{pair} [$R_\mathcal{M}$]	E_{low} [GeV]				
0.5	25	6.6	69	96	71
0.75	20	5.9	85	95	90
0.75	25	5.2	58	96	89
1	15	6	94	93	100
1	20	5.2	95	95	100
1	25	4.6	95	96	98
1.5	20	4.3	99	98	100

Table 1: The values of the percentage of photon showers, which are available for reconstruction, $\wp_\gamma$, and of the acceptance, $\mathcal{A}$, purity, $\mathcal{P}$, and efficiency, $\mathcal{E}$, of the algorithm, for several pairs of merging-cuts on the minimal energy of a cluster, E_{low}, and on the separation distance between a pair of clusters, d_{pair}. The errors on the values are of $\mathcal{O}(0.1\%)$. The merging-cut d_{pair} is expressed in units of the Molière radius, $R_\mathcal{M}$.

The relative error of the effective cross-section as a result of miscounting depends on the observed number of effective leptons and photons, and on the fractions of miscounted events out of the relevant event population. The probability of finding a given value for $N_{1\to2}$ or for $N_{2\to1}$ is given by the binomial distribution, and so the respective relative errors are

$$\left(\frac{\Delta N}{N}\right)_{1\to2} = \frac{\sqrt{N_\ell p_\ell q_\ell}}{N_\ell} = \sqrt{\frac{p_\ell q_\ell}{N_\ell}} \quad \text{and} \quad \left(\frac{\Delta N}{N}\right)_{2\to1} = \frac{\sqrt{N_\gamma p_\gamma q_\gamma}}{N_\gamma} = \sqrt{\frac{p_\gamma q_\gamma}{N_\gamma}}\,, \qquad (11)$$

where $N_{\ell,(\gamma)}$ is the number of effective leptons (photons), $p_{\ell,(\gamma)}$ is the probability to miscount $N_{\ell,(\gamma)}$ in a given event and $q_{\ell,(\gamma)} = 1 - p_{\ell,(\gamma)}$. It is important to distinguish between the two types of errors. While for the sample of $3{\cdot}10^4$ events the values for p_ℓ and for p_γ were both of the same order, the number of instances where there was merging of two showers was smaller than the number of single showers which split ($N_{2\to1} < N_{1\to2}$). This occurred due to the fact that there were less events in which there were multiple showers, which could have merged, to begin with. As a result, the relative error due

to false merging is higher. Practically speaking, each event had the potential for false splitting, since in every event there was at least one shower, but only events where a photon shower was present as well, had the potential for false merging.

Values for $p_{\ell,(\gamma)}$ and for $q_{\ell,(\gamma)}$ were derived by running the clustering algorithm on the sample of Bhabha events with different sets of merging-cuts on E_{low} and d_{pair}. The corresponding relative errors are shown in Table 2. Also shown there is the relative error

$$\left(\frac{\Delta N_{tot}}{N_{tot}}\right)_{500} = \left(\left(\frac{\Delta N}{N}\right)_{1\to 2} \oplus \left(\frac{\Delta N}{N}\right)_{2\to 1}\right)_{500} \quad , \tag{12}$$

which corresponds to the total error resulting from both types of miscounting, rescaled for an integrated luminosity of 500 fb^{-1} .

Cuts		$\frac{\Delta N_{1\to 2}}{N_{1\to 2}}$	$\frac{\Delta N_{2\to 1}}{N_{2\to 1}}$	$\left(\frac{\Delta N_{tot}}{N_{tot}}\right)_{500}$
d_{pair} $[R_{\mathcal{M}}]$	E_{low} [GeV]			
0.5	25	$4.2 \cdot 10^{-4}$	$31.5 \cdot 10^{-2}$	$10.3 \cdot 10^{-5}$
0.75	20	$7.6 \cdot 10^{-4}$	$14.6 \cdot 10^{-2}$	$7.5 \cdot 10^{-5}$
0.75	25	$5.4 \cdot 10^{-4}$	$14.6 \cdot 10^{-2}$	$8 \cdot 10^{-5}$
1	15	$12.9 \cdot 10^{-4}$	$6.3 \cdot 10^{-2}$	$5.1 \cdot 10^{-5}$
1	20	$7 \cdot 10^{-4}$	$4.6 \cdot 10^{-2}$	$4.9 \cdot 10^{-5}$
1	25	$5.1 \cdot 10^{-4}$	$5.2 \cdot 10^{-2}$	$5.3 \cdot 10^{-5}$
1.5	20	$3.2 \cdot 10^{-4}$	$0.5 \cdot 10^{-2}$	$1.8 \cdot 10^{-5}$

Table 2: The relative errors on the miscounting of clusters (using $N_{1\to 2}$ and $N_{2\to 1}$), and the total relative error on the measurement of the effective Bhabha cross-section (using N_{tot}), for several pairs of merging-cuts on the minimal energy of a cluster, E_{low}, and on the separation distance between a pair of clusters, d_{pair}. The merging-cut d_{pair} is expressed in units of the Molière radius, $R_{\mathcal{M}}$. The relative errors of the numbers for miscounted showers, $N_{1\to 2}$ and $N_{2\to 1}$, are computed for a sample of $3{\cdot}10^4$ Bhabha events. The number N_{tot} takes into account both of the miscounting errors, and is computed for an integrated luminosity of 500 fb^{-1}.

It is apparent from Tables 1 and 2 and from Eq. (12) that achieving a minimum of error in counting the number of effective photons depends both on the size of the sample of available photons, and on the sensitivity of the algorithm to miscounting. For merging-cuts in energy ≥ 20 GeV and distance ≥ 1 $R_{\mathcal{M}}$, the algorithm makes relatively

few mistakes. The decision on where exactly to set the merging-cuts reduces to the choice of maximizing the measurable amount of statistics.

5.2.2 Event-by-Event Comparison of Observables

Other than counting the number of low and high-energy clusters and comparing the results to the expected numbers, deduced from the effective Bhabha cross-section, the properties of the clusters may also be evaluated. For this purpose, one may produce such distributions as the production angles of clusters, the angular separation between pairs of clusters, and the value of cluster-energy. A first step in this process is to look at the shower/cluster differences on an event-by-event basis.

The energy of the particle which initiated a generated shower (reconstructed cluster) is determined by integrating all the contributions of the shower (cluster) and multiplying by a calibration constant. The constant transforms between the values of the detector signal and the particle energy, and was found in [20, 25]. Figure 12 shows the relative deviation of the energy of reconstructed clusters and their respective generated showers, as a function of the energy of the generated shower. The deviations are of $\mathcal{O}(2$ GeV) or lower. The reconstructed clusters, which are taken into account here, belong to the effective Bhabha cross-section for which $E_{low} \geq 20$ GeV and $d_{pair} \geq 1\ R_{\mathcal{M}}$. Increasing the merging-cut on separation distance reduces the fluctuations significantly, due to reduced cluster-mixing (as indicated by Fig. 10), but also reduces the available statistics.

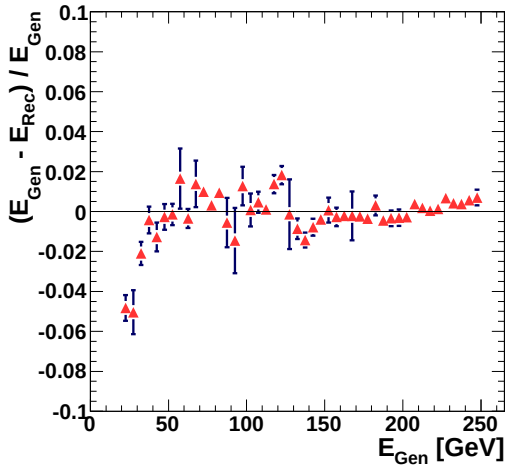

Figure 12: The normalized difference between the energy of generated showers, E_{gen}, and their respective reconstructed clusters, E_{rec}, as a function of the energy of the generated shower.

Figure 13 shows the normalized difference between the position of reconstructed clusters and their respective generated showers. The position is parametrized by the polar angle, θ, and by the azimuthal angle, ϕ. The difference is presented as a function of the energy of the generated shower. Since the fluctuations in all cases are of $\mathcal{O}(10^{-4})$ or lower, it is concluded that the position reconstruction is performed well. This makes sense in light of Eq. (5), since only the core of high energy cells, which are in close proximity to the cluster center, contribute to the position reconstruction. Low-energy cells which are miss-assigned between clusters, therefore, do not degrade the position reconstruction.

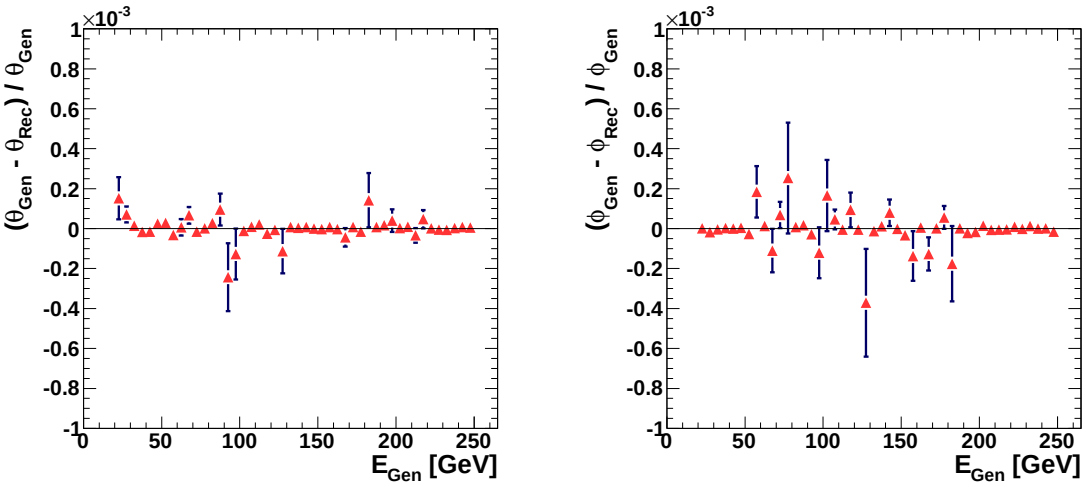

(a) (b)

Figure 13: The normalized difference between the position of generated showers and their respective reconstructed clusters. The position is parametrized by the reconstructed and the generated polar angles, θ_{Rec} and θ_{Gen}, (a) and by the reconstructed and the generated azimuthal angles, ϕ_{Rec} and ϕ_{Gen}, (b) and is presented as a function of the energy of the generated shower, E_{Gen}.

5.2.3 Measurable Distributions

The distribution of the energy of reconstructed clusters and their respective generated showers for high- and low-energy clusters (showers) is shown in Figs. 14a and 14b, respectively.

Figure 15 shows the distributions of the polar angle, θ, of reconstructed clusters and their respective generated showers. The sample is divided into high and low-energy clusters (showers). In Fig. 16 is presented the distribution of the difference in polar

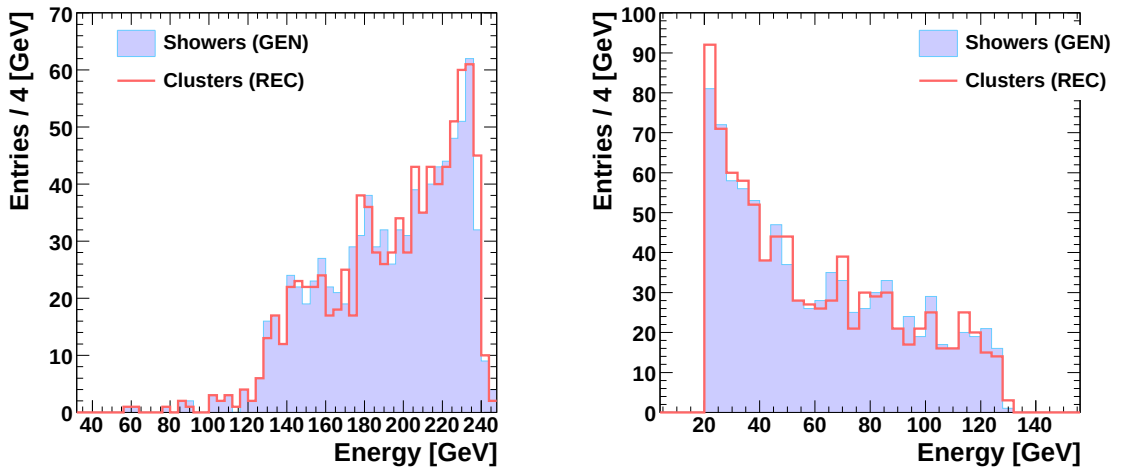

(a) (b)

Figure 14: Distributions of the energy of reconstructed clusters (REC) and their respective generated showers (GEN), as denoted in the figures. The sample is divided into high (a) and low-energy (b) clusters (showers).

angle, $\Delta\theta_{high,low} \equiv \theta_{high} - \theta_{low}$, between the high- and low-energy reconstructed clusters and their respective generated showers.

In light of the relations shown in Fig. 13 one might naively expect that the match between the distributions of cluster and shower positions would be better. The small noticeable discrepancies originate from miscounted events. On a case-by-case basis the difference in reconstruction of the polar and azimuthal angles is usually below the resolving power of LumiCal. However, single showers which are reconstructed as two clusters, and shower pairs that are reconstructed as single clusters, must also be taken into account. The distributions in Fig. 11 indicate that the source of the discrepancies is showers with small angular separation. This is indeed the case, as can be deduced from Fig. 17, where the instances of failure of the algorithm are shown as a function of the separation distance between pairs of showers, d_{pair}, and of the energy of the low-energy shower, E_{low}. The merging-cuts $E_{low} \geq 20$ GeV and $d_{pair} \geq 1\ R_{\mathrm{M}}$ have been used for selection of reconstructed clusters. The algorithm tends to produce mistakes when merging showers for which E_{low} and d_{pair} are close to the merging-cut values, which is due to errors in either the position or the energy reconstruction.

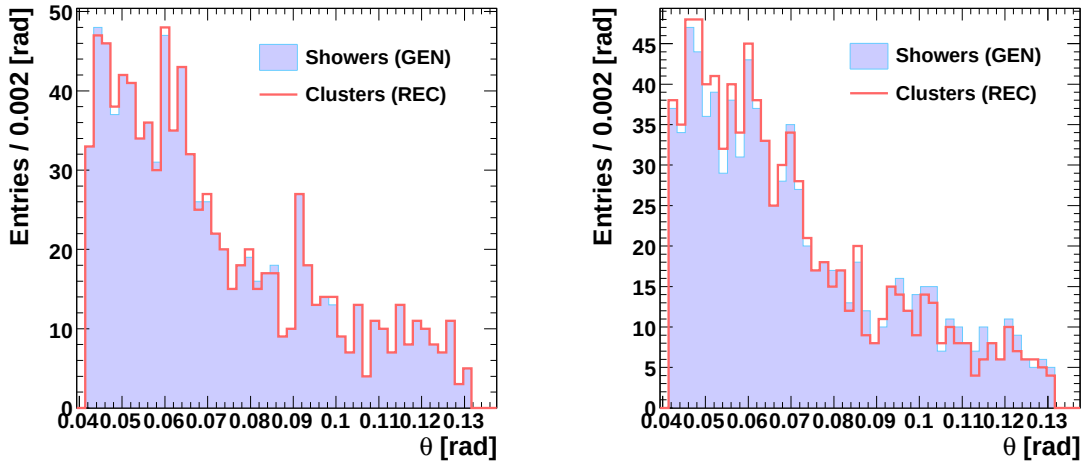

(a) (b)

Figure 15: Distributions of the polar angle, θ, of reconstructed clusters (REC) and their respective generated showers (GEN), as denoted in the figures. The sample is divided into high (a) and low-energy (b) clusters (showers).

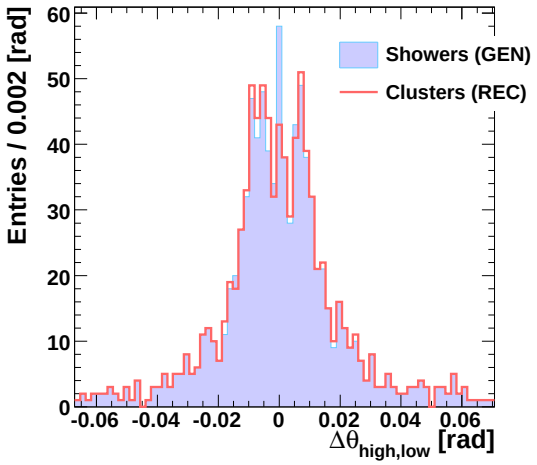

Figure 16: Distributions of the difference in polar angle, $\Delta\theta_{high,low}$, between the high- and low-energy reconstructed clusters (REC) and their respective generated showers (GEN), as denoted in the figure.

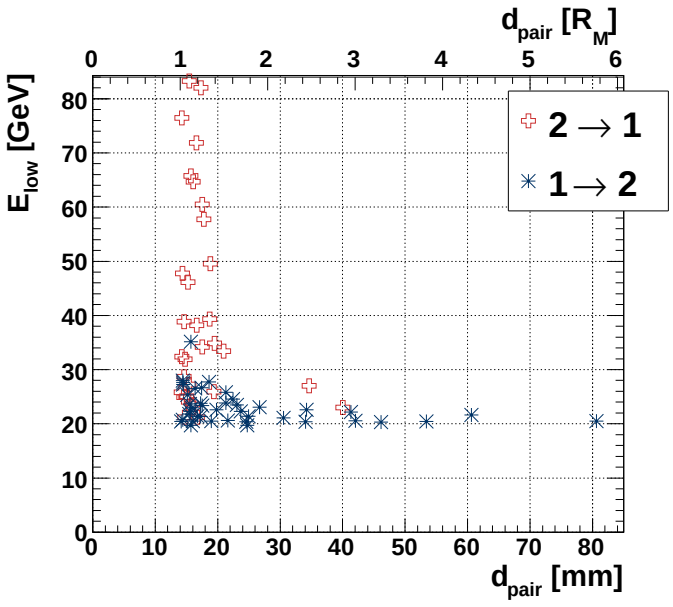

Figure 17: Instances of failure of the clustering algorithm in distinguishing between a pair of generated showers, as a function of the separation distance between the pair, d_{pair}, and of the energy of the low-energy shower, E_{low}. The distance d_{pair} is expressed in units of mm and of the Molière radius, $R_{\mathcal{M}}$. Two cases are possible, a pair of generated showers may be merged into one reconstructed cluster ($2 \rightarrow 1$), or one shower may be separated into two clusters ($1 \rightarrow 2$). The event sample considered complies with the merging-cuts $E_{low} \geq 20$ GeV and $d_{pair} \geq 1\ R_{\mathcal{M}}$.

5.3 Dependence on the Size of LumiCal Cells

The success of the clustering algorithm in measuring the effective Bhabha cross-section, depends on the granularity of LumiCal. The performance, which was presented in Sect. 5.2, was evaluated for a detector with a radial cell size, $\Delta r = 1.1$ mrad, which corresponds to 19% of $R_{\mathcal{M}}$, and an azimuthal cell size, $\Delta\phi = 65.5$ mrad, which corresponds to 37 and 164% of $R_{\mathcal{M}}$ at the inner and outer radii of LumiCal, respectively (see Sect. 2.1). Due to the fact that R&D efforts are continuing, the detector concept is still fluid. Consequently, the restrictions on the size and positioning of LumiCal may change in the future.

In order to estimate the dependence of the performance of the clustering algorithm on these changes, the clustering of a sample of 10^4 Bhabha events was performed for different LumiCal segmentation schemes. The merging cuts used on the minimal energy of a cluster and on the separation distance between a pair of clusters are $E_{low} \geq 20$ GeV and $d_{pair} \geq 1\ R_{\mathcal{M}}$, respectively. The values of the acceptance and purity (Eq. (9)) for the different schemes are presented in Table 3. Also shown is the total relative error on the measurement of the effective Bhabha cross-section (Eqs. (11) and (12)) for an integrated luminosity of 500 fb^{-1}.

One may fine-tune the parameters of the algorithm in order to adjust the values of the acceptance and of the purity. In general, an increase in $\mathcal{A}$ will be followed by a decrease of $\mathcal{P}$, as one is a measure of over-merging of clusters, and the other of under-merging. The contribution to the statistical error of the number of shower-pairs which are reconstructed as one cluster, far outweighs that of the number of single showers which are reconstructed as two clusters. Since it is advisable to choose parameters, such that the total error is minimal, the acceptance tends to be higher than the purity for the examples given in Table 3.

Changes in the number of azimuthal divisions have a large effect on the final error of the cross-section measurement, compared to changes in the number of radial divisions. This difference is due to the fact that LumiCal is more finely granulated in the radial direction. Applying looser merging-cuts for less finely granulated geometries is not recommended. While this may compensate for the decrease in $\mathcal{A}$ and $\mathcal{P}$ that follows the increase in cell size, it also results in a decrease in the number of separable low-energy showers.

6 Summary

It has been shown that it is possible to resolve the distribution of radiative Bhabha photons on top of the electron distribution. Using this measurement, it will be possible to study the influence of the beam-beam effects, and of the energy spread of the collider, on the Bhabha cross-section. In order to achieve results of high acceptance and purity,

Number of Cells		Cell Length				$\mathcal{A}$ [%]	$\mathcal{P}$ [%]	$\left(\frac{\Delta N_{tot}}{N_{tot}}\right)_{500}$
		$\Delta\phi$ ($R_{min} \to R_{max}$)		Δr				
N_ϕ	N_r	[mrad]	$[R_{\mathcal{M}}]$	[mrad]	$[R_{\mathcal{M}}]$			
96	310	65.5	$0.37 \to 1.64$	0.38	0.06	99	94	$2.9 \cdot 10^{-5}$
	78			1.52	0.24	98	92	$3.5 \cdot 10^{-5}$
48	310	131	$0.74 \to 3.28$	0.38	0.06	94	79	$6.6 \cdot 10^{-5}$
	156			0.76	0.12	93	77	$7.5 \cdot 10^{-5}$
	78			1.52	0.24	90	84	$9.1 \cdot 10^{-5}$
24	156	262	$1.48 \to 6.56$	0.76	0.12	76	22	$11.1 \cdot 10^{-5}$

Table 3: The values of the acceptance, $\mathcal{A}$, and purity, $\mathcal{P}$, of the algorithm, for several division schemes, given by the number of azimuthal and radial divisions, N_ϕ and N_r. The azimuthal and radial cell length, $\Delta\phi$ and Δr, are expressed in units of mrad, and of the Molière radius, $R_{\mathcal{M}}$, at the inner and outer radii of LumiCal, $R_{min} \to R_{max} = 80 \to 350$ mm. Also shown is the total relative error on the measurement of the effective Bhabha cross-section for an integrated luminosity of 500 fb^{-1}. The merging-cuts on the minimal energy of a cluster and on the separation distance between a pair of clusters are $E_{low} \geq 20$ GeV and $d_{pair} \geq 1\ R_{\mathcal{M}}$, respectively.

a merging-cut on the minimal energy of each cluster, and on the separation distance between any pair of clusters, needs to be made. The merging leads to a measurement of an effective Bhabha cross-section. The number of effective photons may then be counted with an uncertainty that corresponds to the required precision for the measurement of the luminosity spectrum. The distributions of the position and of the energy of the effective leptons and photons may also be measured and compared to the expected results.

Acknowledgments

This work is partly supported by the Commission of the European Communities under the 6$^{\text{th}}$ Framework Programme "Structuring the European Research Area", contract number RII3-026126, and by the Israeli Science Foundation. We would like to thank Wolfgang Lohmann for his helpful comments and suggestions.

References

[1] K. Mönig, "Physics Needs for the Forward Region." Talk given at the Zeuthen FCAL meeting, Aug. 2004.

[2] T. Becher and K. Melnikov, "Two-loop QED corrections to Bhabha scattering," *arXiv:0704.3582*.

[3] S. Actis, M. Czakon, J. Gluza, and T. Riemann, "Two-loop fermionic corrections to massive Bhabha scattering," *arXiv:0704.2400*.

[4] A. A. Penin, "Two-loop photonic corrections to massive Bhabha scattering," *Nucl. Phys. B 734, 185, arXiv:hep-ph/0508127*, 2006.

[5] M. Czakon, J. Gluza, and T. Riemann, "The planar four-point master integrals for massive two-loop Bhabha scattering," *Nucl. Phys. B 751, 1, arXiv:hep-ph/0604101*, 2006.

[6] S. Jadach, "Theoretical error of the luminosity cross section at LEP," *hep-ph/0306083*, 2003. URL: http://arxiv.org/abs/hep-ph/0306083.

[7] M. Caffo *et al.*, "Bhabha Scattering," *Z Physics at LEP1, CERN Report 89-08, 1*, 1989. URL: http://documents.cern.ch/cgi-bin/setlink?base=cernrep&categ=Yellow_Report&id=89-08_v1.

[8] A. Stahl, "Luminosity Measurement via Bhabha Scattering: Precision Requirements for the Luminosity Calorimeter," *LC-DET-2005-004*, 2005. URL: http://www-flc.desy.de/lcnotes/notes/LC-DET-2005-004.ps.gz.

[9] R. Ingbir, "A Luminosity Detector for the International Linear Collider." URL: http://alzt.tau.ac.il/~ronen/, 2006.

[10] H. Abramowicz *et al.*, "A Luminosity Detector for the International Linear Collider," *LC-DET-2007-006*, 2007. URL: http://www-flc.desy.de/lcnotes/notes/LC-DET-2007-006.pdf.

[11] C. Rimbault *et al.*, "Impact of beam-beam effects on precision luminosity measurements at the ILC," *JINST 2 P09001*, 2007. URL: http://www.iop.org/EJ/abstract/1748-0221/2/09/P09001.

[12] M. N. Frary and D. J. Miller, "Monitoring the Luminosity Spectrum," *DESY-92-123A, 379*, 1991. URL: http://www.hep.ucl.ac.uk/lc/documents/frarymiller.pdf.

[13] K. Mönig, "Measurement of the Differential Luminosity using Bhabha events in the Forward-Tracking region at TESLA," *LC-PHSM-2000-60-TESLA*, 2000. URL: http://www-flc.desy.de/lcnotes/.

[14] "TELSA Technical Design Report," *ECFA-2001-209*, 2001. URL: http://arxiv.org/PS_cache/hep-ph/pdf/0106/0106315v1.pdf.

[15] H. Abramowicz *et al.*, "Redefinition of the Geometry of the Luminosity Calorimeter," *EUDET-Memo-2008-09*, 2008. URL: http://www.eudet.org.

[16] "MOKKA - a detailed GEANT4 detector simulation for the Future Linear Collider." URL: http://polywww.in2p3.fr/geant4/tesla/www/mokka/mokka.html.

[17] J. Allison *et al.*, "GEANT4 developments and applications," *IEEE Transactions on Nuclear Science 53, No. 1, 270-278*, 2006.

[18] "MARLIN - a C++ software framework for ILC software." URL: http://ilcsoft.desy.de/portal/software_packages/marlin/index_eng.html.

[19] T. C. Awes *et al.*, "A simple method of shower localization and identification in laterally segmented calorimeters," *Nucl. Inst. Meth. A311, 130*, 1992.

[20] I. Sadeh, "Luminosity Measurement at the International Linear Collider." URL: http://alzt.tau.ac.il/~sadeh/mscThesis/iftachSadeh_mscThesis.pdf, 2008.

[21] W.-M. t. Yao, "Review of Particle Physics," *Journal of Physics G 33*, 2006. URL: http://pdg.lbl.gov.

[22] B. Rossi, *High Energy Particles, Prentice-Hall, Inc., Englewood Cliffs, NJ*, 1952.

[23] URL: http://alzt.tau.ac.il/~sadeh.

[24] S. Jadach, W. Placzek, and B. F. L. Ward, "BHWIDE 1.00: O(alpha) YFS exponentiated Monte Carlo for Bhabha scattering at wide angles for LEP1/SLC and LEP2," *Phys. Lett. B390, 298-308*, 1997. URL: http://arxiv.org/pdf/hep-ph/9608412.

[25] H. Abramowicz *et al.*, "Revised Requirements on the Readout of the Luminosity Calorimeter," *EUDET-Memo-2008-08*, 2008. URL: http://www.eudet.org.